Available online at www.sciencedirect.com

ScienceDirect

Defence Technology 12 (2016) 334–342

www.elsevier.com/locate/dt

Dimensional analysis and extended hydrodynamic theory applied to long-rod penetration of ceramics

J.D. CLAYTON *

Impact Physics RDRL-WMP-C, US Army Research Laboratory, Aberdeen Proving Ground, Aberdeen, MD 21005-5066, USA
A. James Clark School of Engineering, University of Maryland, College Park, MD 20742, USA

Received 19 January 2016; revised 18 February 2016; accepted 19 February 2016

Available online 15 March 2016

Abstract

Principles of dimensional analysis are applied in a new interpretation of penetration of ceramic targets subjected to hypervelocity impact. The analysis results in a power series representation – in terms of inverse velocity – of normalized depth of penetration that reduces to the hydrodynamic solution at high impact velocities. Specifically considered are test data from four literature sources involving penetration of confined thick ceramic targets by tungsten long rod projectiles. The ceramics are AD-995 alumina, aluminum nitride, silicon carbide, and boron carbide. Test data can be accurately represented by the linear form of the power series, whereby the same value of a single fitting parameter applies remarkably well for all four ceramics. Comparison of the present model with others in the literature (e.g., Tate's theory) demonstrates a target resistance stress that depends on impact velocity, linearly in the limiting case. Comparison of the present analysis with recent research involving penetration of thin ceramic tiles at lower typical impact velocities confirms the importance of target properties related to fracture and shear strength at the Hugoniot Elastic Limit (HEL) only in the latter. In contrast, in the former (i.e., hypervelocity and thick target) experiments, the current analysis demonstrates dominant dependence of penetration depth only by target mass density. Such comparisons suggest transitions from microstructure-controlled to density-controlled penetration resistance with increasing impact velocity and ceramic target thickness.
Production and hosting by Elsevier B.V. on behalf of China Ordnance Society.

Keywords: Ceramics; Terminal ballistics; Armor; Dimensional analysis; Hydrodynamics

1. Introduction

Ceramic materials are of keen interest for use in modern armor systems because of their high hardness, high stiffness, and relatively low mass density relative to traditional armor steels, for example. As reviewed in Reference 1, ceramic materials have been considered for personal and vehicular protection systems since the mid 20th century. Popular candidate ceramics for such systems include alumina, aluminum nitride, boron carbide, silicon carbide, and titanium diboride, among others (e.g., transparent spinels [2] and glass [3]). Despite significant research progress, precise relationships among (micro)structures, properties, and dynamic performance of these often complex materials remain undefined or even contradictory among collective findings of the engineering mechanics, materials science, and condensed matter physics communities.

A number of different experimental methods have been devised over the past six decades that probe properties or performance of ceramic materials at very high rates of loading pertinent to armor applications. These experiments involve impact and/or penetration of ceramic targets and commensurate shock wave propagation, progressive material degradation, and material failure. Two particular experimental target configurations are of primary interest in this work. The first, as explained in detail in References 4 and 5, consists of one or more ceramic tiles backed by a semi-infinite metal block. Performance of the ceramic armor tiles is measured by the depth of penetration of the projectile, often either a metallic bullet or rather short rod, into the backing metal. The second, also described in Reference 4 as well as References 6 and 7 involves thick (effectively semi-infinite) cylindrical ceramic targets confined laterally, with or without a metallic cover plate. Performance of the thick ceramic is measured via depth of penetration of the projectile, often a metallic long rod. Dwell and interface defeat may be observed if the projectile velocity is too low to enable penetration into a hard, confined ceramic [7].

Peer review under responsibility of China Ordnance Society.

* Tel.: 410 278 6146.
E-mail address: john.d.clayton1.civ@mail.mil, jdclayt1@umd.edu (J.D. CLAYTON).

http://dx.doi.org/10.1016/j.dt.2016.02.004
2214-9147/Production and hosting by Elsevier B.V. on behalf of China Ordnance Society.

A vast ensemble of models have been developed, often in conjunction with experimental methods, for describing the mechanical response of armor ceramics. These can be organized in terms of scale of resolution. Quantum mechanical representations incorporating density functional theory [8,9] have enabled quantification of fundamental elastic and fracture properties of ceramic crystals and interfaces, as have empirical lattice statics/dynamics calculations [10]. Mesoscale calculations [11–13] incorporating cohesive finite elements [14–16] or phase field representations [17,18] enable description of the effects of microstructure such as grain sizes and orientations on the response of ceramic polycrystals. Macroscopic constitutive models are used in hydrocodes for computing the response of protection systems subjected to impact, blast, and perforation. These models may be empirical [19–23] or based on micromechanical principles [24–26]. One-dimensional finite crystal mechanics models have also been developed for addressing planar shock experiments [27–31]. Finally, analytical penetration models based on a one-dimensional momentum balance and various simplifying assumptions have been invoked to describe mechanics of shaped charge jets [32–34] and long rods [35–38] piercing thick ductile metallic targets. These models, which tend to reduce to a Bernoulli-type equation at the stagnation point of impact, will be critically reviewed later in the present work.

The present paper provides a new description of penetration of semi-infinite ceramic targets by metallic long-rod projectiles using dimensional analysis with application to literature data [6,39–41]. This paper extends prior recent work [5] that addressed, in an empirical manner, the first experimental configuration discussed above, i.e., metal-backed ceramic tiles. The present work includes new comparison of dimensional analysis with some one-dimensional penetration theories [35,36,42] for example providing contextual insight into the target resistance term in Tate's model [36], now applied for ceramic targets. Another goal is possible elucidation of the effects of differences, or lack thereof, among ceramic material properties (inherently related to microstructure) on penetration resistance.

The main body of this paper is structured as follows. In §2, one-dimensional penetration mechanics models are reviewed, including key assumptions and governing equations. In §3, dimensional analysis of the problem of penetration of thick ceramic targets is performed. In §4, application of this dimensional analysis to test data is reported. In §5, further analysis and comparison of the present results with one-dimensional penetration mechanics models and other experimental configurations are undertaken. Conclusions follow in §6.

2. One-dimensional penetration mechanics

Presented next in §2.1 is a derivation of the governing equation for ideal hydrodynamic penetration of a semi-infinite target by a jet or rod. This derivation provides a basis for the extended descriptions and more elaborate models discussed in §2.2.

2.1. Ideal hydrodynamic theory

The ideal hydrodynamic theory of penetration of ductile targets by shaped charge jets was developed around the Second World War and years soon thereafter [32]. The assumptions involved in the derivation are listed as follows: the penetration process is steady-state and one-dimensional; the target is semi-infinite; the projectile is a continuous jet; and both target and jet materials are incompressible with null shear strength, thereby acting as perfect fluids.

Let spatial coordinates at time t be denoted by $x_i = x_i(X_I, t)$, where reference coordinates of a material point are X_I and in general, $i, I = 1, 2, 3$. Particle velocity is

$$v_i(X_I, t) = \frac{\partial x_i(X_I, t)}{\partial t} \tag{1}$$

Let σ_{ij} denote the symmetric Cauchy stress tensor, and $p = -\frac{1}{3}\sigma_{ii}$ the Cauchy pressure. Let ρ denote the spatial mass density. The local balance of linear momentum in continuum mechanics is [43]

$$\frac{\partial \sigma_{ij}}{\partial x_j} = \rho \frac{\partial v_i(X_I, t)}{\partial t} \tag{2}$$

In a Cartesian coordinate system, the particle acceleration is the following material time derivative of the velocity

$$\frac{\partial v_i(X_I, t)}{\partial t} = \frac{\partial v_i(x_j, t)}{\partial t} + \frac{\partial v_i(x_j, t)}{\partial x_j}\frac{\partial x_j(X_I, t)}{\partial t} \tag{3}$$

For steady flow, $v_i = v_i(x_j)$ and the first term on the right side of Equation (3) vanishes, leading to

$$\frac{\partial v_i(X_I, t)}{\partial t} = \frac{\partial v_i(x_j)}{\partial x_j} v_j = v_j \frac{\mathrm{d}v_i}{\mathrm{d}x_j} \tag{4}$$

For steady one-dimensional flow, $i, I = 1$ and Equation (2) becomes, with $\sigma(x) = -\sigma_{11}(x)$ the axial stress, positive in compression,

$$-\frac{1}{\rho}\frac{\mathrm{d}\sigma}{\mathrm{d}x} = v\frac{\mathrm{d}v}{\mathrm{d}x} \Rightarrow -\frac{\mathrm{d}\sigma}{\rho} = v\mathrm{d}v \tag{5}$$

Now assume that a jet or rod with initial velocity V impinges on the target, an infinite half-space. The stagnation point between projectile and target recedes with velocity U. The axial stress P at the stagnation point in the projectile is then found by integrating Equation (5) with ρ_0 the projectile density, which is assumed constant for incompressible flow, leading to [44]

$$-\int_0^P \mathrm{d}\sigma = \rho_0 \int_{V-U}^0 v\mathrm{d}v \Rightarrow P = \frac{1}{2}\rho_0 (V-U)^2 \tag{6}$$

Now considering the stagnation point in the target, which is assumed incompressible with mass density ρ_T,

$$-\int_0^P \mathrm{d}\sigma = \rho_T \int_U^0 v\mathrm{d}v \Rightarrow P = \frac{1}{2}\rho_T U^2 \tag{7}$$

Equating P from Equations (6) and (7), and letting $p = P$ for inviscid flow (no shear stresses), Bernoulli's equation for steady hydrodynamic penetration is

$$p = P = \frac{1}{2}\rho_0 (V-U)^2 = \frac{1}{2}\rho_T U^2 \tag{8}$$

The time needed for a projectile of initial length L_0 to fully erode is $t_0 = L_0 / (U-V)$, and the depth of penetration is $P_0 = U \cdot t_0$. Using Equation (8), the normalized depth of penetration can be expressed completely in terms of the ratio of densities of target and projectile

$$\frac{P_0}{L_0} = \frac{U}{U-V} = \sqrt{\frac{\rho_0}{\rho_T}} \tag{9}$$

Though originally developed for penetration of metallic targets by metallic jets, this model has been used, often with success, for describing the steady penetration regime for long-rod projectiles as well as brittle targets. Regardless, it serves as a useful basis of comparison with experimental data and predictions of more complex theories and/or numerical calculations.

2.2. Extended penetration models

Many analytical penetration mechanics models have used the hydrodyamic theory derived in §2.1 as a foundation or starting point. Birkhoff et al. [32] accounted for jet particulation via incorporation of a shape factor λ that has a value of one for continuous jets and two for dispersed particle jets

$$\lambda\rho_0 (V-U)^2 = \rho_T U^2 \Rightarrow \frac{P_0}{L_0} = \sqrt{\frac{\lambda\rho_0}{\rho_T}} \tag{10}$$

Pack and Evans [33,45] extended Equation (9) to allow for secondary penetration (i.e., afterflow in addition to primary penetration) r as well as an empirical correction for target strength Y_T

$$\frac{P_0}{L_0} = \sqrt{\frac{\lambda\rho_0}{\rho_T}}\left(1 - a\frac{Y_T}{\rho_0 V^2}\right) + \frac{r}{L_0} \tag{11}$$

Here a is permitted to depend on target and jet densities, and $aY_T / (\rho_0 V^2) = kR$, with k an empirical factor and R the work per unit volume required for crater formation. Eichelberger [42] added to Equation (8) a statistical factor γ and the net strength difference $Y_N = Y_T - Y_0$, with Y_0 the jet strength

$$\gamma\rho_0 (V-U)^2 = \rho_T U^2 + 2Y_N \tag{12}$$

In the late 1960s, Alekseevski [35] and Tate [36] independently derived theories for long-rod penetration of metallic targets that considered deceleration of the rod due to strengths of both projectile (Y_0) and target (R_T). The governing equation for equal stresses in target and projectile at the stagnation point can be derived by modifying the limits of integration in Equations (6) and (7) such that steady flow does not commence until the stress reaches the strength/resistance of either material

$$-\int_{Y_0}^{P} \mathrm{d}\sigma = \rho_0 \int_{V-U}^{0} v\,\mathrm{d}v \Rightarrow P = \frac{1}{2}\rho_0 (V-U)^2 + Y_0 \tag{13}$$

$$-\int_{R_T}^{P} \mathrm{d}\sigma = \rho_T \int_{U}^{0} v\,\mathrm{d}v \Rightarrow P = \frac{1}{2}\rho_T U^2 + R_T \tag{14}$$

Equating axial stresses P then gives Tate's extended Bernoulli equation

$$\frac{1}{2}\rho_0 (V-U)^2 + Y_0 = \frac{1}{2}\rho_T U^2 + R_T \tag{15}$$

The complete theory developed in References 35 and 36 includes differential equations for projectile deceleration and erosion that must be integrated numerically to obtain depth of penetration, except in very special/simple cases. However, if deceleration is ignored, then the analytical solution for penetration depth is

$$\frac{P_0}{L_0} = \frac{U}{U-V} = \frac{1}{\mu}\left(\frac{\mu\sqrt{V^2 + A} - V}{\mu V - \sqrt{V^2 + A}}\right) \tag{16}$$

where

$$\mu = \sqrt{\rho_T / \rho_0}, \qquad A = 2\left(1-\mu^2\right)\left(R_T - Y_0\right) / \rho_T \tag{17}$$

The same result can be recovered from Equation (12) when $\gamma \to 1$ and $Y_N \to R_T - Y_0$. Notice that Equation (16) reduces to the hydrodynamic result of Equation (9) for very high velocities or low material strengths, i.e., for $V^2 \gg A$.

In Reference 46, the description of long-rod penetration was extended to account for a transition from plastic deformation to fluid flow at the head of the rod, with a transition velocity derived depending on rod strength. In Reference 47, the governing Equation (15) for the steady penetration phase was re-derived in the context of an assumed flow field for a perfectly plastic target. Extension of the analysis to phases of unsteady impact, plastic-wave dominated, and after-flow was presented [48]. Numerical simulations [49] predicted that the entrance phase of penetration provides little net effect on penetration efficiency, while the end phase dominates overshoot of the hydrodynamic limit for ductile metals subjected to hypervelocity impact.

More elaborate analytical models considering momentum exchange that relax assumptions of Tate's original theory were derived in References 34, 37 and 50; the latter [50] compares analytical predictions with numerical results for metal rods penetrating metal targets, demonstrating that target resistance R_T depends on the experimental configuration as well as target material properties.

Walker and Anderson [38] derived a time-dependent model for unsteady long-rod penetration of semi-infinite targets. This model considers initial impact (requiring an initial interface velocity from the shock jump conditions) as well as rod deceleration; assumptions are made on the plastic flow field in the target (from a dynamic cavity expansion analysis) and velocity profile in the projectile (from observations in numerical simulations). For a limiting case, the analogy of Tate's target resistance was found to vary with the dynamic ratio β of plastic zone size to cavity size, which decreases with increasing velocity V for metallic targets

$$R_T = \frac{7}{3} Y_T \ln[\beta(V)] \tag{18}$$

A dimensional analysis of simulation results [51] for metals showed that larger-scale targets tend to be weaker than their small-scale counterparts due to rate and time-to-failure effects, since longer times are available for damage mechanisms (shear bands, fractures, etc.) to incubate and propagate in larger targets. This phenomenon was also observed in experiments of penetration of layered ceramic–metal systems [52]. Experiments and hydrocode simulations showed importance of strengths of both target and projectile over a range of impact velocities, with strength effects increasing with decreasing impact velocity [53]. Simulations also demonstrated a relatively small effect of compressibility on penetration for very ductile metallic targets except at very high velocities [54].

In another analysis of long-rod impact data, a two-regime model was developed to study the transition from plastically deforming rods to eroding penetration [55]. Recently, a three-regime model has been used to address the transition from rigid, to non-eroding but deforming, to eroding, long rods with increasing impact velocity [56]. Both of the latter two mentioned approaches are most relevant for rod materials of higher strength than target materials (e.g., tungsten impacting aluminum [55]) and less so for hypervelocity impact of metal projectiles into harder ceramic targets of current interest [6,39–41] wherein rod erosion dominates the nearly steady penetration process.

3. Dimensional analysis: general

Buckingham's pi theorem is now applied toward dimensional analysis of mechanics of long-rod penetration. Buckingham's pi theorem applied to any physical system can be described generically as follows [57–59]. See also the discussion on similitude concepts in Reference 60. If an equation involving n variables is dimensionally homogeneous, it can be reduced to an equation among $n - k$ independent dimensionless products, with k being the number of independent reference dimensions needed to characterize all of the variables. In dimensional, rather than dimensionless form, let

$$y = f(x_2, x_3, \ldots, x_n) \tag{19}$$

where y is the dependent variable and $x_2, \ldots, x_n$ are independent quantities, some of which may be independent variables and others constants in a given problem. Equation (19) can be converted to dimensionless form as

$$\Pi_1 = \varphi(\Pi_2, \Pi_3, \ldots, \Pi_{n-k}) \tag{20}$$

where Π_1 is the dimensionless analog of y and function φ depends on $n - k - 1$ of other dimensionless products (i.e., pi terms) constructed from the original set $\{y, x_2, x_3, \ldots, x_n\}$. Normalization of all variables entering φ should, for convenience, be completed via only the set $\{x_2, x_3, \ldots, x_n\}$ such that independent variable y appears only once, on the left side of the governing equation.

In this paper, the ballistic penetration problem to which Buckingham's theorem is applied is illustrated in Fig. 1. The experimental set-up, as discussed for example in References 4, 6, 7, 39–41, consists of a rod of initial length L_0 impacting a thick (effectively semi-infinite) ceramic target at velocity V_0, with the cylindrical ceramic target encased in a metallic sleeve and cover plate that provide confinement. The experiment is performed in reverse ballistic fashion, meaning that the ceramic target package is launched at the rod in a light gas gun. The present analysis is restricted to normal impact, i.e., in principle null obliquity. Performance of the ceramic target is measured by residual penetration depth P_0, with penetration resistance decreasing with increasing P_0.

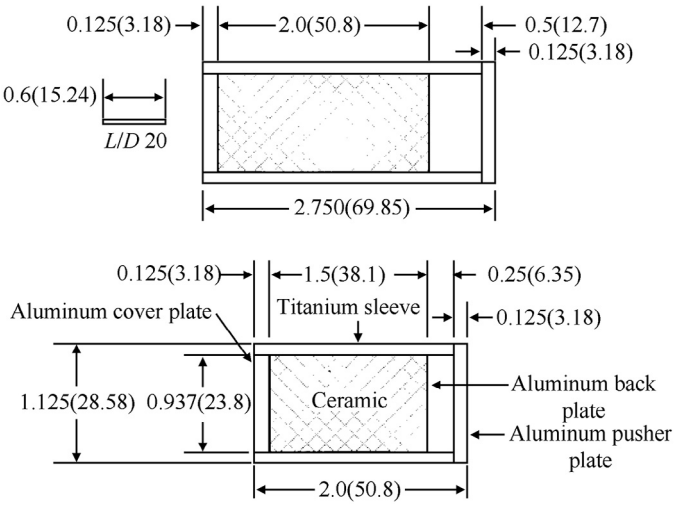

Fig. 1. Reverse ballistic experiment. Long-rod penetration into encased thick ceramic target(s); dimensions in inches (mm). Reproduced from Reference 6 with permission from Elsevier Science.

In dimensional form, penetration depth is expressed as the following function of impact velocity, geometric variables $\{g\}$, and material property variables $\{m\}$, letting respective subscripts 0 and T denote penetrator, ceramic target

$$P_0 = P_0(V_0, \{g\}_0, \{m\}_0, \{g\}_T, \{m\}_T) \tag{21}$$

Possible lateral and frontal confinement is included in the set of target geometric variables. In subsequent analysis, application/fitting of Equation (21) is restricted to experimental data sets for which the projectile and target geometries remain fixed or nearly so. Further letting $\{g\}_0 \to L_0$, Equation (21) reduces under these assumptions to

$$P_0 = P_0(V_0, L_0, \{m\}_0, \{m\}_T) \tag{22}$$

A reduced form of Equation (22) is required in the context of dimensional analysis. Presumably, this reduced equation should satisfy the following conditions: (i) it should be a dimensionless function of dimensionless quantities, (ii) it should yield the penetration depth into a perfect inviscid and incompressible fluid as $V_0 \to \infty$, and (iii) it should satisfy observed physics of the problem, notably a decreasing primary penetration depth with decreasing V_0 relative to the ideal hydrodynamic solution given by Equation (9), as will be demonstrated explicitly in the context of experimental results analyzed later in §4. In order to satisfy these requirements with minimal complexity, the following material parameters are introduced: the strength Y_0 of the projectile, the

Table 1
Ballistic penetration experiments.

Experiment	D_0 / mm	L_0/D_0	V_0 / (km·s^{-1})	Target material	$\beta_0, \beta_1, \beta_2, \beta_3$	R_T / GPa	α
Subramanian & Bless [6]	0.762	20	1.5–3.5	Alumina (Al_2O_3)	4.871, −6.375, 2.995, −0.407	7.0–9.0	3.6
Orphal et al. [39]	0.762	20, 15	1.5–4.5	Aluminum nitride (AlN)	−1.258, 1.842, −0.342, 0.022	5.0–9.0	2.9
Orphal & Franzen [40]	0.762	20, 15	1.5–4.6	Silicon carbide (SiC)	0.747, −0.049, 0.185, −0.024	5.0–9.0	3.1
Orphal et al. [41]	0.762, 1.02	20, 15	1.5–5.0	Boron carbide (B_4C)	−1.213, 2.178, −0.512, 0.044	5.0–9.0	2.9

mass densities of the projectile and target ρ_0 and ρ_T, and a series of z dimensionless constants $\alpha_l, l = 0, 1, 2, \ldots, z$ that potentially depend only on the target material (i.e., type of ceramic). In other words, $\{m\}_0 \to \{\rho_0, Y_0\}$ and $\{m\}_T \to \{\rho_T, \alpha_l\}$. In dimensional form, Equation (22) then becomes

$$P_0 = P_0[V_0, L_0; \rho_0, Y_0; \rho_T, \alpha_l (l = 0, 1, 2, \ldots, z)] \tag{23}$$

Each application of Equation (23) is further restricted to data sets for which the penetrator's geometry is fixed, such that $L_0 = \text{constant}$ is used only to normalize P_0 as is conventional in analysis of ballistic data [4,37,51] and, e.g., in Equation (9). The now-posited dimensionless form [requirement (i)] of the penetration depth equation is

$$\frac{P_0}{L_0} = \varphi\left(\sqrt{\frac{\rho_T}{\rho_0}}, \sqrt{\frac{Y_0}{\rho_0 V_0^2}}, \alpha_l\right) = \varphi(\mu, \chi, \alpha_l) \tag{24}$$

Recall μ is first defined in Equation (17). Dimensionless variable $\chi = \sqrt{Y_0 / (\rho_0 V_0^2)}$, a function only of penetrator characteristics, is defined here. In the context of Buckingham's theorem, three independent dimensions (mass, length, and velocity) enter the variables considered in Equation (23), so $k = 3$. The total number of pi terms is $n = 7 + z$, and the number of independent dimensionless terms is thus $n - k - 1 = 3 + z$, consistent with the number of independent variables on the right side of dimensionless Equation (24). Requirement (ii) implies

$$(P_0 / L_0)_\infty = \varphi(\mu, 0, \alpha_l) = \varphi_\infty(\mu) = 1/\mu \tag{25}$$

where φ_∞ is the dimensionless penetration depth in the limit of infinite impact velocity ($\chi \to 0$) given by Equation (9). Requirement (iii) suggests a power series in χ of the following form

$$\frac{P_0}{L_0} = \varphi = \frac{1}{\mu}\sum_{l=0}^{z} \alpha_l \chi^l = \sqrt{\frac{\rho_0}{\rho_T}}\left(1 + \alpha_1\sqrt{\frac{Y_0}{\rho_0 V_0^2}} + \alpha_2 \frac{Y_0}{\rho_0 V_0^2} + \cdots\right) \tag{26}$$

where $\alpha_0 = 1$ to satisfy Equation (25). Note that if $z = 1$, then $\alpha_1 < 0$ to satisfy requirement (iii). Application of Equation (26) to data in §4 demonstrates that $z = 1$ is sufficient to describe penetration depth over hypervelocity impact regimes for ceramic materials and target configurations of present interest, as will be shown explicitly later. Notice also that making particular choices $\alpha_1 = 0, \alpha_2 = -aY_T / Y_0$ recovers the form in Equation (11) [33] in the absence of secondary penetration ($r = 0$), for steady projectile velocity ($V_0 = V$) and a continuous projectile ($\lambda = 1$).

4. Dimensional analysis: application to experimental data

The dimensional analysis framework developed in §3 is now applied to the experimental penetration data of Subramanian and Bless [6] and Orphal et al. [39–41]. As mentioned already in the context of Fig. 1, all such reverse ballistic experiments involve long-rod hypervelocity impact and penetration into confined cylindrical ceramic targets. Important characteristics of experiments reported in each reference are listed in Table 1. Projectile properties are listed in Table 2, corresponding to relatively pure polycrystalline tungsten. The strength value $Y_0 = 2.0$ GPa is consistent with that used in References 39–41 and dynamic yield reported in Reference 14. With a few exceptions, most experiments consider long rods with length-to-diameter ratios of $L_0/D_0 = 20$; impact velocities V_0 range from 1.5 to 5.0 km/s. Target resistance values R_T entering Equation (15) as reported in the experimental references are listed in the rightmost column of Table 1.

Normalized primary penetration depths are fit to cubic equations in References 39–41 with corresponding fitting parameters $\beta_i, (i = 0, 1, 2, 3)$ listed in Table 1

$$P_0 / L_0 = \beta_0 + \beta_1 V_0 + \beta_2 V_0^2 + \beta_3 V_0^3, \qquad [V_0 \text{ in km / s}] \tag{27}$$

The same cubic equation is also used to fit alumina data of Reference 6, with parameters β_i determined newly here by regression. Also listed in Table 1 is the value of dimensionless parameter α_1 of Equation (26) used to fit the experimental data

$$\frac{P_0}{L_0} = \frac{1}{\mu}\left(\alpha_0 + \alpha_1 \frac{\sqrt{Y_0/\rho_0}}{V_0} + \cdots\right) \simeq \frac{1}{\mu}\left(1 - \alpha \frac{\sqrt{Y_0/\rho_0}}{V_0}\right) \tag{28}$$
$$[\alpha_0 = 1; \alpha_1 = -\alpha]$$

As demonstrated in the context of Figs. 2, 3, 4, and 5, truncation of Equation (26) at order one (i.e., a linear fit with respect to inverse impact velocity) is sufficient to accurately fit

Table 2
Projectile material properties.

Material	Density ρ_0 /(g·cm^{-3})	Strength Y_0/GPa	Structure	Inelasticity	Reference
Tungsten (W)	19.3	2.0	Body-centered-cubic	Slip, fracture	[14]

Table 3
Representative ceramic material properties.

Material	Density ρ_T/(g·cm^{-3})	Modulus E/GPa	Poisson ratio ν	Tough K_C / MPa$\sqrt{m}$	Compress σ_C / GPa	Bend σ_B / GPa	Hard H_V/GPa	HEL σ_H/GPa	Dyn. str. 2τ / GPa	Structure c, a / nm	Inelastic deformation	References
Al_2O_3	3.89	373	0.23	4.5	2.6	0.38	14.1	7.6	5.3	Trigonal 1.3, 0.5	Slip, twinning	[27,61–63]
AlN	3.24	315	0.24	2.7	2.1	0.35	11.5	9.4	6.0	Hexagonal 0.5, 0.3	Slip, phase change	[24,64,65]
SiC	3.22	453	0.16	5.1	3.4	0.40	27.4	15.7	11.4	Hexagonal 1.5, 0.3	Slip	[25,61,66]
B_4C	2.51	461	0.17	3.1	2.8	0.40	31.4	16.0	7.1	Trigonal 1.2, 0.6	Amorphization	[61,66,67]

all experimental data. Specifically, α is fit to each experimental data set by minimizing the error

$$\text{Error} = \int \left[\left| (P_0)_{\text{model}} - (P_0)_{\text{cubic}} \right| / (P_0)_{\text{cubic}} \right] dV_0 \tag{29}$$

where $(P_0)_{\text{model}}$ is given by Equation (28) and $(P_0)_{\text{cubic}}$ by Equation (27), and the domain of integration corresponds to velocity ranges listed in Table 1. Also considered later is a universal fit of Equation (28) with a single best value of $\alpha = 3.0$ obtained by minimizing the sum of errors [computed using Equation (29)] for all four data sets involving four different ceramic target materials.

Properties of ceramic materials comprising each target are given for reference in Table 3. Initial mass density ρ_T, elastic (Young's) modulus E, Poisson's ratio ν, fracture toughness K_C, compressive strength σ_C, bending strength σ_B, and Vicker's hardness H_V are static material properties. The Hugoniot Elastic Limit (HEL) σ_H and dynamic shear strength τ of the shocked ceramic – the latter defined in Reference 61 from the intersection of the elastic line with the failed strength curve of the shocked material – are dynamic properties. Lattice parameters are a and c. Variations among ceramics' properties – which are intrinsically related to their microstructures – are common as evidenced by ranges reported in Reference 68, for example. All of these ceramics undergo fracture when subjected to dynamic loading of sufficient magnitude; other known inelastic deformation mechanisms are listed in the second column from the right, where slip and twinning refer to dislocation glide and mechanical twinning [43], respectively. The phase change in AlN occurs at pressures around 20 GPa. Amorphization in B_4C is a stress-induced change from trigonal crystal structure to a non-crystalline solid phase [16].

Experiments and model fits are compared in Fig. 2 for alumina, Fig. 3 for aluminum nitride, Fig. 4 for silicon carbide, and Fig. 5 for boron carbide. Raw data points are included in Fig. 2 since these are tabulated in Reference 6; data points are not tabulated in other experimental sources [39–41] and hence are not included in corresponding Figs. 3, 4, and 5. Importantly, for each material, the fit using a universal value of $\alpha = 3.0$ is very nearly as accurate as that which minimizes the error (Equation 29) for each material individually. As reported in References 6,39–41, the following features also characterize most experiments analyzed here: the penetration process is steady; the relationship between target velocity U and projectile velocity V is usually linear; the relationship between penetration depth and time is usually linear; the rod is completely eroded by the end of each experiment; some secondary penetration occurs, such that the total penetration depth exceeds the primary penetration depth. Notice from Figs. 2, 3, 4, and 5 that the hydrodynamic limit penetration depth of Equation (9) is approached with increasing V_0 but is never achieved for any target configuration over the range of impact velocities consid-

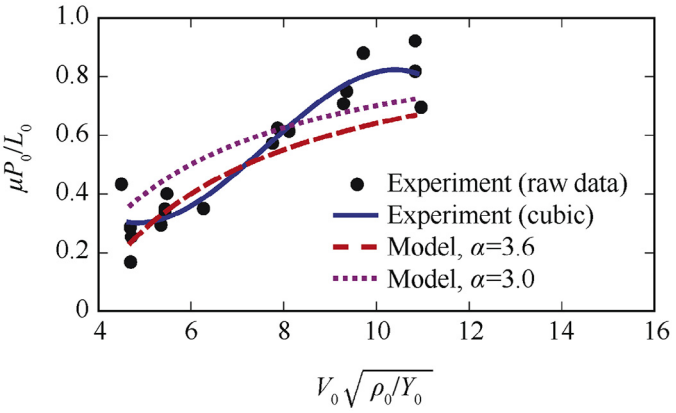

Fig. 2. Aluminum oxide. Comparison of experimental results – raw data of Reference 6 and cubic fit (Equation 27) – with those of the presently proposed dimensionless model (Equation 28). Hydrodynamic limit penetration depth is $\mu P_0/L_0 = 1$ (see Equation 9).

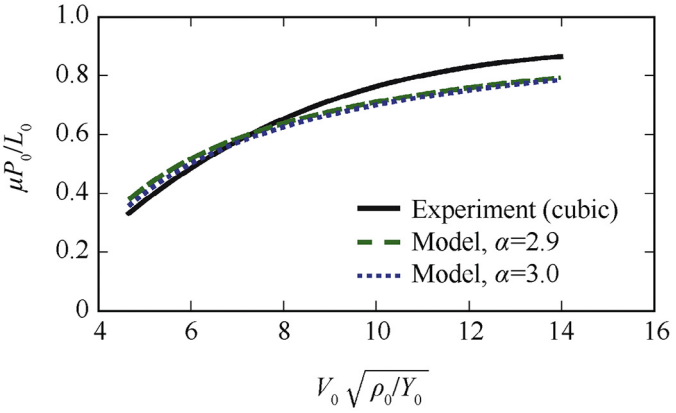

Fig. 3. Aluminum nitride. Comparison of experimental results – cubic fit of Reference 39 and Equation (2) – with those of the presently proposed dimensionless model (Equation 28). Hydrodynamic limit penetration depth is $\mu P_0/L_0 = 1$ (see Equation 9).

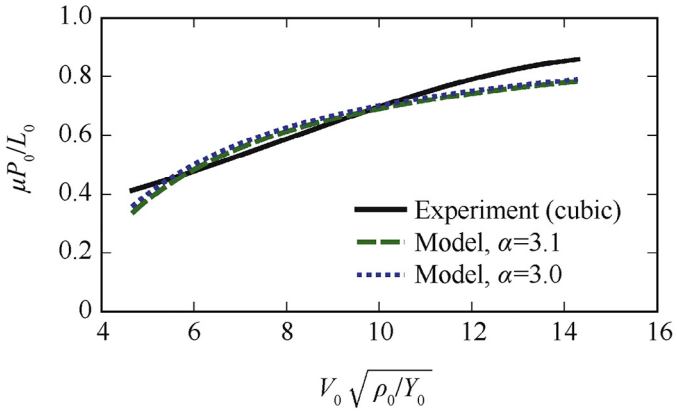

Fig. 4. Silicon carbide. Comparison of experimental results – cubic fit of Reference 40 and Equation (27) – with those of the presently proposed dimensionless model (Equation 28). Hydrodynamic limit penetration depth is $\mu P_0/L_0 = 1$ (see Equation 9).

ered. Setting $P_0/L_0 = 0$ in Equation (28) results in the following limit velocity below which penetration should not occur

$$(V_0)_{\text{limit}} = \alpha\sqrt{Y_0/\rho_0} \tag{30}$$

With $\alpha = 3$ and tungsten rod properties of Table 2, the predicted limit velocity is 0.97 km/s for the present target–projectile combinations. It is cautioned, however, that the present analysis has only been verified for impact velocities at or exceeding $V_0 = 1.5$ km/s, so this limit is an obvious extrapolation of the model in Equation (28).

5. Further analysis and discussion

The primary discovery of the present work is that normalized penetration data for all four ceramic target materials – alumina, aluminum nitride, silicon carbide, and boron carbide – can be described well using new dimensionless Equation (28) with a single fitting parameter, α, taking a universal value of 3.0. With α thus independent of target material, penetration depth depends only on the (fixed) properties of the projectile (Y_0 and ρ_0) and the density of the ceramic target which enters the ratio $\mu = \sqrt{\rho_T/\rho_0}$. With this supposition in place, static and dynamic strength properties and mechanisms listed in Table 3 would seem to be of little influence on penetration depth for the present test configuration, since otherwise α would tend to vary among materials with different physical properties, underlying microstructures, and dominant deformation mechanisms. Furthermore, α would seem to be unrelated to dynamic viscosity of the ceramic material, since penetration depth results reported for aluminum nitride [39] and boron carbide [41] suggest similar trends for larger-scale tests. If α were to depend on viscosity or failure kinetics, then test results would not demonstrate such scaling since larger scale tests involve longer time scales and lower average strain rates [51]. Instead, α must depend on ceramic/target properties that do not vary strongly with material type or with average strain rate. Such properties are unresolved at present, and further speculation on the physical origin of resistance parameter α is not supported by the existing results. In future work, parametric numerical simulations wherein material properties can be varied systematically and at low cost should provide further insight.

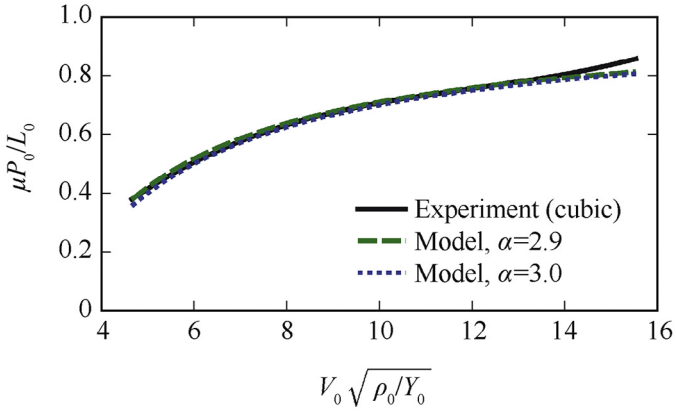

Fig. 5. Boron carbide. Comparison of experimental results – cubic fit of Reference 41 and Equation (27) – with those of the presently proposed dimensionless model (see Equation 28). Hydrodynamic limit penetration depth is $\mu P_0/L_0 = 1$ (see Equation 9).

Comparison of the present findings with those of a recent dimensional analysis [5] of a different target configuration and velocity regime is in order. The latter configuration, as explained in References 4 and 5, consists of one or more ceramic tiles backed by a semi-infinite metal block. Performance is measured by the depth of penetration of the projectile into the backing metal. In Reference 5, dimensional analysis determined that penetration of rather thin, metal-backed ceramic tiles could be described by two parameters that do depend on the type of ceramic material. The first, needed for describing the effect of ceramic tile thickness, was found to be associated with the ratio of surface energy (i.e., fracture toughness) to elastic modulus. The second, needed to describe the relationship between penetration depth and impact velocity, was related to the ratio of dynamic shear strength τ to target density. Impact velocities ranged from 0.6 to 3.0 km/s, and projectiles had typical L_0/D_0 ratios on the order of 4 [69]. In contrast, the present experiments involve thick, confined ceramic targets (effectively semi-infinite) with somewhat longer projectiles and higher impact velocities, with penetration depth depending primarily on target material only through its mass density. Therefore, comparison of the dimensional analysis reported here and in Reference 5 suggests a transition from fracture- and dynamic strength-controlled target resistance to mass density-controlled target resistance with increasing impact velocity and ceramic target thickness or confinement.

It is instructive to consider the present penetration depth Equation (28) in the context of models of Eichelberger, Alekseevskii, and Tate [35,36,42]. Define $R_N = R_T - Y_0$ as a net target–projectile resisting stress. Then Equation (15) can be written

$$\rho_0(V-U)^2 = \rho_T U^2 + 2R_N \tag{31}$$

which is very similar to Equation (12) when $\gamma = 1$. Using the series expansion $1/\sqrt{1+2x} = 1 - x + \frac{3}{2}x^2 - \cdots$, normalized penetration depth for steady penetration throughout the entire

time of target–projectile interaction ($V = V_0$) is then calculated as

$$\frac{P_0}{L_0} = \frac{U}{U-V} = \left(\frac{\rho_0 U^2}{\rho_T U^2 + 2R_N}\right)^{1/2} = \sqrt{\frac{\rho_0}{\rho_T}}\left(\frac{U^2}{U^2 + 2R_N/\rho_T}\right)^{1/2} = \frac{1}{\mu}\left(\frac{1}{1+2R_N/(\rho_T U^2)}\right)^{1/2} \approx \frac{1}{\mu}\left(1-\frac{R_N}{\rho_T U^2}\right) \tag{32}$$

Then, equating like terms in Equations (28) and (32) gives, with $\alpha = -\alpha_1$,

$$\frac{R_N}{\rho_T U^2} = \alpha\frac{\sqrt{Y_0/\rho_0}}{V} \Rightarrow R_N = \alpha\mu\sqrt{\rho_T Y_0}\frac{U^2}{V} \tag{33}$$

Successive approximations $U \approx \kappa V \approx \frac{1}{1+\mu}V$ [70] result in a linear dependence of target resistance on velocity if Y_0 is presumed constant

$$R_T = R_N + Y_0 \approx \alpha\mu\sqrt{\rho_T Y_0}\kappa^2 V + Y_0 \approx \alpha\sqrt{Y_0/\rho_0}\frac{\rho_T}{(1+\mu)^2}V + Y_0 \tag{34}$$

This result, which relies on linearization and several intermediate mathematical reductions, can be positively compared with the experimental results for silicon carbide and boron carbide [40,41], which show a nonlinearly increasing relation between R_N and impact velocity, and contrasted with the Walker–Anderson theory in Equation (18) that predicts, for ductile metallic targets, a decreasing R_T with increasing impact velocity. The ceramic-dependent term in the last of Equation (34), $\rho_T/(1+\mu)^2$, varies only from 1.35 to 1.85 g/cm^3 for the different target materials considered herein. Therefore, consistent with experimental findings, a nearly constant value of α among all four ceramics to be used in Equation (34) correlates well with the very similar ranges of target resistance $R_T \approx 5.0$–9.0 GPa reported in experiments for all four ceramics as listed in Table 1.

For thick ceramic targets impacted at high velocities, the present analysis, as noted above, suggests that primary penetration depth P_0 depends on ceramic type almost exclusively on mass density ρ_T, specifically via $P_0 \propto \rho_T^{-1/2}$. Consider two target tiles of different ceramic materials of the same surface area. The ratio of masses of the two tiles is directly proportional to the ratio of areal densities $\rho_T \cdot h$, with h the thickness. Now assume that h is sufficient to enable semi-infinite conditions as addressed by the analysis herein, with each tile of the same (large) thickness. Then the ratio of penetration depths into the two different targets should scale simply and inversely with ratio of square roots of masses of the two targets.

It should be emphasized that the present analysis, including the main result given by Equation (28) with $\alpha = 3$ for all four ceramics considered, applies most strictly only for tests in which projectile and target geometries and projectile material are held fixed. Furthermore, impact velocities to which the analysis holds are restricted to the range 1.5–5.0 km/s. Target materials are strong ceramics, such that penetration conditions are steady and eroding. Additional experiments and corresponding analysis are required to verify or refute the use of Equation (28) for other test conditions.

6. Conclusions

Dimensional analysis has been invoked in a new study of ballistic penetration of ceramic materials. In particular, data considered here involve primary penetration depths into thick ceramic targets of alumina (high purity), aluminum nitride, silicon carbide, and boron carbide struck by tungsten long rods at impact velocities spanning 1.5–5.0 km/s. Data sets from four independent experimental investigations from the literature have been analyzed.

Application of Buckingham's pi theorem in conjunction with several physical assumptions has resulted in a dimensionless penetration depth depending on projectile mass density and strength, target mass density, and a power series of dimensionless parameters in terms of inverse impact velocity. The test data have been accurately fit using only the first (linear) term in this series, with a single value of the corresponding dimensionless fitting parameter used successfully for all four ceramic target materials when other aspects of the test configuration (e.g., penetrator and target dimensions) are held fixed in an experimental series. Comparison with one-dimensional extensions to hydrodynamic theory has demonstrated a dependence of Tate's target resistance on impact velocity, where a linear relation applies to first order. Consideration of the current results with those of prior dimensional analysis of thin, metal-backed ceramic targets confirms existence of a transition from fracture- and strength-controlled resistance to mass density-controlled resistance with increasing average impact velocity and target thickness.

References

[1] Walley SM. Historical review of high strain rate and shock properties of ceramics. Adv Appl Ceram 2010;109:446–66.
[2] Clayton JD. A nonlinear thermomechanical model of spinel ceramics applied to aluminum oxynitride (AlON). J Appl Mech 2011;78:011013.
[3] Walley SM. An introduction to the properties of silica glass in ballistic applications. Strain 2014;50:470–500.
[4] Rosenberg Z, Dekel E. Terminal ballistics. Berlin: Springer; 2012.
[5] Clayton JD. Penetration resistance of armor ceramics: dimensional analysis and property correlations. Int J Impact Eng 2015;85:124–31.
[6] Subramanian R, Bless SJ. Penetration of semi-infinite AD995 alumina targets by tungsten long rod penetrators from 1.5 to 3.5 km/s. Int J Impact Eng 1995;17:807–16.
[7] Lundberg P, Renstrom R, Lundberg B. Impact of metallic projectiles on ceramic targets: the transition between interface defeat and penetration. Int J Impact Eng 2000;24:259–75.
[8] Taylor DE. Shock compression of boron carbide: a quantum mechanical analysis. J Am Ceram Soc 2015;98:3308–18.
[9] Beaudet TD, Smith JR, Adams JW. Surface energy and relaxation in boron carbide ($10\bar{1}1$) from first principles. Solid State Commun 2015;219:43–7.
[10] Kenway PR. Calculated stacking-fault energies in α-Al_2O_3. Philos Mag B 1993;68:171–83.
[11] Clayton JD, McDowell DL. A multiscale multiplicative decomposition for elastoplasticity of polycrystals. Int J Plasticity 2003;19:1401–44.
[12] Bourne NK. Impact on alumina. I. Response at the mesoscale. Proc R Soc Lond A 2006;462:3061–80.
[13] Leavy RB, Clayton JD, Strack OE, Brannon RM, Strassburger E. Edge on impact simulations and experiments. In: Procedia engineering, vol. 58. Elsevier; 2013. p. 445–52.
[14] Clayton JD. Dynamic plasticity and fracture in high density polycrystals: constitutive modeling and numerical simulation. J Mech Phys Solids 2005;53:261–301.

[15] Kraft RH, Molinari JF. A statistical investigation of the effects of grain boundary properties on transgranular fracture. Acta Mater 2008;56:4739–49.
[16] Clayton JD, Kraft RH, Leavy RB. Mesoscale modeling of nonlinear elasticity and fracture in ceramic polycrystals under dynamic shear and compression. Int J Solids Struct 2012;49:2686–702.
[17] Clayton JD, Knap J. A phase field model of deformation twinning: nonlinear theory and numerical simulations. Physica D 2011;240:841–58.
[18] Clayton JD, Knap J. Phase field modeling of directional fracture in anisotropic polycrystals. Comp Mater Sci 2015;98:158–69.
[19] Holmquist TJ, Johnson GR. Response of silicon carbide to high velocity impact. J Appl Phys 2002;91:5858–66.
[20] Johnson GR, Holmquist TJ, Beissel SR. Response of aluminum nitride (including a phase change) to large strains, high strain rates, and high pressures. J Appl Phys 2003;94:1639–46.
[21] Leavy RB, Brannon RM, Strack OE. The use of sphere indentation experiments to characterize ceramic damage models. Int J Appl Ceram Tech 2010;7:606–15.
[22] Clayton JD. Modeling and simulation of ballistic penetration of ceramic-polymer-metal layered systems. Math Probl Eng 2015;2015:709498.
[23] Riegel JP, Davison D. Consistent constitutive modeling of metallic target penetration using empirical, analytical, and numerical penetration models. Defence Technol 2016;12:202–14.
[24] Curran DR, Seaman L, Cooper T, Shockey DA. Micromechanical model for comminution and granular flow of brittle material under high strain rate application to penetration of ceramic targets. Int J Impact Eng 1993;13:53–83.
[25] Clayton JD. Deformation, fracture, and fragmentation in brittle geologic solids. Int J Fracture 2010;163:151–72.
[26] Tonge AL, Ramesh KT. Multi-scale defect interactions in high-rate brittle material failure. Part I: model formulation and application to ALON. J Mech Phys Solids 2016;86:117–49.
[27] Clayton JD. A continuum description of nonlinear elasticity, slip and twinning, with application to sapphire. Proc R Soc Lond A 2009;465:307–34.
[28] Clayton JD. Nonlinear Eulerian thermoelasticity for anisotropic crystals. J Mech Phys Solids 2013;61:1983–2014.
[29] Clayton JD. Analysis of shock compression of strong single crystals with logarithmic thermoelastic-plastic theory. Int J Eng Sci 2014;79:1–20.
[30] Clayton JD. Finite strain analysis of shock compression of brittle solids applied to titanium diboride. Int J Impact Eng 2014;73:56–65.
[31] Clayton JD, Tonge AL. A nonlinear anisotropic elastic–inelastic constitutive model for polycrystalline ceramics and minerals with application to boron carbide. Int J Solids Struct 2015;64–65:191–207.
[32] Birkhoff G, MacDougall DP, Pugh EM, Taylor G. Explosives with lined cavities. J Appl Phys 1948;19:563–82.
[33] Pack DC, Evans WM. Penetration by high-velocity (‘Munroe’) jets: I. Proc Phys Soc B 1951;64:298–302.
[34] Walters WP, Majerus JN. Impact models for penetration and hole growth. Technical Report ARBRL-TR-2069, Ballistic Research Laboratory, Aberdeen Proving Ground, MD; 1978.
[35] Alekseevskii VP. Penetration of a rod into a target at high velocity. Combust Explos Shock Waves 1966;2(2):63–6.
[36] Tate A. A theory for the deceleration of long rods after impact. J Mech Phys Solids 1967;15:387–99.
[37] Wright TW. A survey of penetration mechanics of long rods. In: Brebbia CA, Orszag SA, editors. Lecture notes in engineering: computational aspects of penetration mechanics, vol. 3. Berlin: Springer-Verlag; 1983. p. 85–106.
[38] Walker JD, Anderson CE. A time-dependent model for long-rod penetration. Int J Impact Eng 1995;16:19–48.
[39] Orphal DL, Franzen RR, Piekutowski AJ, Forrestal MJ. Penetration of confined aluminum nitride targets by tungsten long rods at 1.5–4.5 km/s. Int J Impact Eng 1996;18:355–68.
[40] Orphal DL, Franzen RR. Penetration of confined silicon carbide targets by tungsten long rods at impact velocities from 1.5 to 4.6 km/s. Int J Impact Eng 1997;19:1–13.
[41] Orphal DL, Franzen RR, Charters AC, Menna TL, Piekutowski AJ. Penetration of confined boron carbide targets by tungsten long rods at impact velocities from 1.5 to 5.0 km/s. Int J Impact Eng 1997;19:15–29.
[42] Eichelberger RJ. Experimental test of the theory of penetration by metallic jets. J Appl Phys 1956;27:63–8.
[43] Clayton JD. Nonlinear mechanics of crystals. Dordrecht: Springer; 2011.
[44] Herrmann W, Wilbeck JS. Review of hypervelocity penetration theories. Int J Impact Eng 1987;5:307–22.
[45] Evans WM, Pack DC. Penetration by high-velocity (‘Munroe’) jets: II. Proc Phys Soc B 1951;64:303–10.
[46] Tate A. A possible explanation for the hydrodynamic transition in high speed impact. Int J Mech Sci 1977;19:121–3.
[47] Tate A. Long rod penetration models – part I. A flow field model for high speed long rod penetration. Int J Mech Sci 1986;28:535–48.
[48] Tate A. Long rod penetration models – part II. Extensions to the hydrodynamic theory of penetration. Int J Mech Sci 1986;28:599–612.
[49] Partom Y. On the hydrodynamic limit of long rod penetration. Int J Impact Eng 1997;20:617–25.
[50] Anderson CE, Walker JD. An examination of long-rod penetration. Int J Impact Eng 1991;11:481–501.
[51] Anderson CE, Mullin SA, Kuhlman CJ. Computer simulation of strain-rate effects in replica scale model penetration experiments. Int J Impact Eng 1993;13:35–52.
[52] Anderson CE, Mullin SA, Piekutowski AJ, Blaylock NW, Poormon KL. Scale model experiments with ceramic laminate targets. Int J Impact Eng 1996;18:1–22.
[53] Anderson CE, Orphal DL, Franzen RR, Walker JD. On the hydrodynamic approximation for long-rod penetration. Int J Impact Eng 1999;22:23–43.
[54] Anderson CE, Orphal DL. An examination of deviations from hydrodynamic penetration theory. Int J Impact Eng 2008;35:1386–92.
[55] Segletes SB. The erosion transition of tungsten-alloy long rods into aluminum targets. Int J Solids Struct 2007;44:2168–91.
[56] Lou J, Zhang Y, Wang Z, Hong T, Zhang X, Zhang S. Long-rod penetration: the transition zone between rigid and hydrodynamic penetration modes. Defence Technol 2014;10:239–44.
[57] Buckingham E. On physically similar systems: illustrations of the use of dimensional equations. Phys Rev 1914;4:345–76.
[58] Bridgman PW. Dimensional analysis. New Haven: Yale University Press; 1922.
[59] Sedov LI. Similarity and dimensional methods in mechanics. London: Academic Press; 1959.
[60] Rayleigh L. The principle of similitude. Nature 1915;95:66–8, 202–203, 644.
[61] Bourne NK. The relation of failure under 1D shock to the ballistic performance of brittle materials. Int J Impact Eng 2008;35:674–83.
[62] Senf H, Strassburger E, Rothenhausler H, Lexow B. The dependency of ballistic mass efficiency of light armor on striking velocity of small caliber projectiles. In: Proceedings 17th international symposium on ballistics, vol. 3. Midrand, South Africa; 1998. p. 199–206.
[63] Karandikar PG, Evans G, Wong S, Aghajanian MK. A review of ceramics for armor applications. Ceram Eng Sci Proc 2009;29:163–75.
[64] Hu G, Chen CQ, Ramesh KT, McCauley JW. Mechanisms of dynamic deformation and dynamic failure in aluminum nitride. Acta Mater 2012;60:3480–90.
[65] Anton RJ, Subhash G. Dynamic Vickers indentation of brittle materials. Wear 2000;239:27–35.
[66] Holmquist TJ, Rajendran AM, Templeton DW, Bishnoi KD. A ceramic armor material database. Technical Report 13754, US Army TARDEC, Warren, MI; 1999.
[67] Clayton JD. Towards a nonlinear elastic representation of finite compression and instability of boron carbide ceramic. Philos Mag 2012;92:2860–93.
[68] Ernst H-J, Hoog K. Protective power of several ceramics correlated to some static material parameters. In: Proceedings 13th international symposium on ballistics, vol. 3. Stockholm, Sweden; 1992. p. 119–26.
[69] Reaugh JE, Holt AC, Wilkins ML, Cunningham BJ, Hord BL, Kusubov AS. Impact studies of five ceramic materials and pyrex. Int J Impact Eng 1999;23:771–82.
[70] Anderson CE, Riegel JP. A penetration model for metallic targets based on experimental data. Int J Impact Eng 2015;80:24–35.